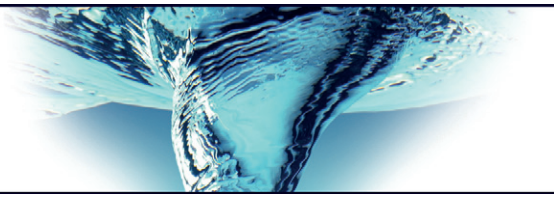
J. Fluid Mech. (2018), *vol.* 843, R1, doi:10.1017/jfm.2018.215



JFM RAPIDS
journals.cambridge.org/rapids

Settling-driven instability in two-component stably stratified Hele-Shaw flows

Rafael M. Oliveira[1] **and Eckart Meiburg**[2,†]

[1]Departamento de Engenharia Mecânica, Pontifícia Universidade Católica do Rio de Janeiro, Rio de Janeiro, RJ 22451-900, Brazil

[2]Department of Mechanical Engineering, University of California at Santa Barbara, Santa Barbara, CA 93106, USA

(Received 26 January 2018; revised 1 March 2018; accepted 5 March 2018; first published online 22 March 2018)

We investigate the onset of instability in a stably stratified two-component fluid in a vertical Hele-Shaw cell when the unstably stratified scalar has a settling velocity. This linear stability problem is analysed on the basis of Darcy's law, for constant-gradient base states. The settling velocity is found to trigger a novel instability mode characterized by pairs of inclined waves. For unequal diffusivities, this new settling-driven mode competes with the traditional double-diffusive mode. Below a critical value of the settling velocity, the double-diffusive elevator mode dominates, while, above this threshold, the inclined waves associated with the settling-driven instability exhibit faster growth. The analysis yields neutral stability curves and allows for the discussion of various asymptotic limits.

Key words: double diffusive convection, Hele-Shaw flows, stratified flows

1. Introduction

If the density of a stably stratified fluid depends on two scalars that diffuse at different rates, and if one of these scalars is unstably stratified, double-diffusive instabilities may arise (Turner 1985; Radko 2013). Examples include the 'salt-fingering' observed when warm salty water overlies cold fresh water and the 'oscillatory convection' that occurs in the reverse configuration. Double-diffusive instabilities are thought to be responsible for significant vertical mixing in the world's oceans (Ruddick & Richards 2003), and they are influential in such diverse contexts as magma dynamics, the formation of stars (Traxler, Garaud & Stellmach 2011) and industrial applications.

Double-diffusive convection can furthermore be important within porous environments, such as for the dynamics of geothermal basins or with regard to CO_2

† Email address for correspondence: meiburg@engineering.ucsb.edu

© Cambridge University Press 2018

https://doi.org/10.1017/jfm.2018.215 Published online by Cambridge University Press

sequestration (Tsai, Riesing & Stone 2013). Griffiths (1981) explored this flow regime by performing Hele-Shaw experiments that showed the ratio of the buoyancy fluxes to be proportional to the square root of the diffusivity ratio. Employing a salt–sugar system to study double-diffusive fingering in porous media, Imhoff & Green (1988) found the vertical sugar transport to be two orders of magnitude larger than that due to molecular diffusion alone. For a stable salinity stratification in a porous layer heated from below, Murray & Chen (1989) measured a dramatic increase in the heat flux compared with single-component convection. Cooper, Glass & Tyler (1997) conducted experiments to test the applicability of stability criteria for double-diffusive fingering convection, while Cooper, Glass & Tyler (2001) investigated the effect of the buoyancy ratio on these flows. Pringle & Glass (2002) explored the effect of the concentration level for fixed buoyancy ratios, while Pringle, Glass & Cooper (2002) focused on the temporal and spatial development of double-diffusive fingers. Nield (1968) performed a linear stability analysis for a horizontal layer of a saturated porous medium to quantify oscillatory convection as function of the thermal and solute Rayleigh numbers. Taunton, Lightfoot & Green (1972) extended Nield's investigation to salt-fingering convection, while Karimi-Fard, Charrier-Mojtabi & Mojtabi (1999) explored the onset of convection in a tilted porous cavity. Rudraiah, Srimani & Friedrich (1982) considered the linear and nonlinear stability of a two-component fluid in a saturated porous layer. A comprehensive review of double-diffusive convection in porous media is provided by Nield & Bejan (2017).

Very recently, Alsinan, Meiburg & Garaud (2017) addressed the stability of stably stratified two-component fluids governed by the Navier–Stokes equations, when the unstably stratified scalar gives rise to a settling velocity. Such situations may be encountered in the context of sediment transport, for example when a buoyant plume of sediment-laden freshwater is situated above denser salt water. The authors identified a novel instability mode driven by this settling velocity that gives rise to the growth of inclined waves, even if both scalars have identical diffusivities. For unequal diffusivities, this settling-driven instability mode competes with the traditional double-diffusive instability. Reali *et al.* (2017) performed corresponding three-dimensional direct numerical simulations. These exhibited the formation of horizontal layers, whose existence was attributed to a secondary instability.

In the current investigation, we explore the influence of a settling velocity on the stability of two-component stably stratified fluids in vertical Hele-Shaw cells. This scenario is of interest in the context of hydraulic fracturing, where particulate proppants are injected into narrow vertical rock fractures (Valko & Economides 1995). In these narrow rock fractures, inertial forces are likely to be important close to the injection point, but, deeper into the fracture, we expect the frictional forces from the sidewalls to dominate, so that Darcy's law should be applicable.

We analyse the linear stability based on Darcy's law, along with convection–diffusion equations for the temperature and sediment-concentration fields. The analysis demonstrates the existence of a settling-driven instability mode also for Hele-Shaw flows, corresponding to the finding by Alsinan *et al.* (2017) for Navier–Stokes flows. We investigate the competition between this settling-driven instability mode and the traditional double-diffusive mode as a function of the governing dimensionless parameters. For vanishing settling velocities and lateral base state gradients, the current stability analysis reduces to the one of Rudraiah *et al.* (1982), if the inertial terms in their analysis are neglected. Neutral stability curves are discussed, along with various asymptotic behaviours.

https://doi.org/10.1017/jfm.2018.215 Published online by Cambridge University Press

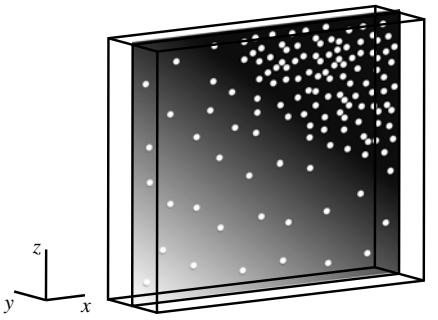


FIGURE 1. Schematic representation of a two-component stratified fluid in a vertical Hele-Shaw cell. Darker shading indicates higher temperature, and white dots represent settling particles.

2. Physical problem

As base state, we consider a stably stratified incompressible Newtonian fluid at rest in a vertical Hele-Shaw cell, as shown in figure 1. The density of the fluid varies linearly in the vertical direction as a result of a stabilizing temperature gradient and a destabilizing sediment-concentration gradient. The sediment is characterized by a Stokes settling velocity and a constant diffusivity. We perform a linear stability analysis based on Darcy's law, along with convection–diffusion equations for the temperature and sediment-concentration fields,

$$\boldsymbol{u} = -\boldsymbol{\nabla} p + Ra(T - C)\hat{\boldsymbol{k}}, \tag{2.1}$$

$$\frac{\partial T}{\partial t} + \boldsymbol{u} \cdot \boldsymbol{\nabla} T = \nabla^2 T, \tag{2.2}$$

$$\frac{\partial C}{\partial t} + \boldsymbol{u} \cdot \boldsymbol{\nabla} C - W_{st} \frac{\partial C}{\partial z} = \tau \nabla^2 C, \tag{2.3}$$

$$\boldsymbol{\nabla} \cdot \boldsymbol{u} = 0. \tag{2.4}$$

In the above dimensionless equations, $\boldsymbol{u} = (u, w)$ indicates the gap-averaged fluid velocity, p is the pressure, $\hat{\boldsymbol{k}}$ denotes the unit vector in the direction of gravity, and T and C represent the temperature and sediment-concentration fields respectively. Here, we assume that the density ρ depends linearly on T and C

$$\rho = 1 - \alpha(T - T_m) + \beta(C - C_m), \tag{2.5}$$

where T_m and C_m denote reference values, while α and β indicate constant expansion coefficients.

The governing equations and the base state give rise to five dimensionless parameters,

$$Ra = \frac{\alpha b^4 T_{0z} \rho_m g}{12 \mu \kappa_T}, \quad \tau = \frac{\kappa_c}{\kappa_T}, \quad W_{st} = \frac{W_{st}^* b}{\kappa_T}, \quad R_\rho = \frac{\alpha T_{0z}}{\beta C_{0z}}, \quad \phi = \frac{T_{0x}}{T_{0z}}. \tag{2.6a–e}$$

These are obtained by introducing characteristic scales for length, time, velocity, temperature and sediment concentration respectively, in the form $[d] = b$, $[t] = b^2/\kappa_T$,

https://doi.org/10.1017/jfm.2018.215 Published online by Cambridge University Press

$[v] = \kappa_T/b$, $[T] = T_{0z}b$ and $[C] = \alpha T_{0z}b/\beta$. Here, b denotes the gap width of the Hele-Shaw cell, while κ_T and κ_C indicate the thermal and sediment diffusivities respectively. The parameter Ra represents a thermal Rayleigh number, which can be interpreted as the ratio of the pressure gradient due to the base state temperature gradient, $\alpha T_{0z} b \rho_m g$, and a flow-induced pressure gradient, $12\mu\kappa_T/b^3$. The parameter τ indicates the diffusivity ratio, and W_{st} represents the Stokes settling velocity. The density ratio R_ρ arises from the base state profiles for the temperature and sediment concentration, T_0 and C_0. The parameter ϕ accounts for linear horizontal gradients in the base state temperature and sediment-concentration profiles, which are assumed to be density-compensating, so that $\alpha T_{0x} = \beta C_{0x}$,

$$T_0(x, z) = \phi x + z; \quad C_0(x, z, t) = \phi x + \frac{1}{R_\rho}(z + W_{st}t). \tag{2.7a,b}$$

Realistic values of the governing parameters can be estimated along the following lines. The thermal diffusivity of water at room temperature is $\kappa_T = 0.145 \times 10^{-6}$ m^2 s^{-1}, the thermal expansion coefficient can be taken as $\alpha = 2 \times 10^{-4}$ K^{-1}, and T_{0z}, in °C m^{-1}, can range from $O(10^{-2})$ to $O(1)$. In fact, in vertical fissures created by hydraulic fracturing, temperature gradients can change drastically, and variations between $T_{0z} = -0.8$ °C m^{-1} and $T_{0z} = 2.7$ °C m^{-1} have been recorded (Dobkins 1981). Following Reali *et al.* (2017), the settling velocity can be estimated as $W_{st} = (b/\kappa_T)W^*_{st} = (b/\kappa_T)((2r^2(\rho_p - \rho_m)g)/9\mu)$, where r denotes the particle radius. The reference density, ρ_m, can vary from 800 kg m^{-3} to 1200 kg m^{-3}, spanning different materials such as oils, water and glycerin. On the other hand, ρ_p may range from 1200 kg m^{-3} to 3900 kg m^{-3}. It may represent the density of sediments, such as sand or clay, or of proppants used in hydraulic fracturing operations. These can comprise a variety of materials such as walnut shells, plastic, hollow glass, silica sand, resin-coated sand, ceramics and sintered bauxite (Liang *et al.* 2016). The dynamic viscosity can range from $\mu = 1$ mPa s to $\mu = 1000$ mPa s for oils or water–glycerin stable solutions. Based on these values, and considering gap sizes between 0.1 and 1 mm, the dimensionless settling velocity can be estimated as a function of the particle radius, r. It can range from values as low as $W_{st} \approx 10^{-10}$ to as high as $W_{st} \approx 500$ for particle sizes from colloidal size to hundreds of microns. This provides the motivation for analysing the influence of this parameter across several orders of magnitude.

The diffusivity ratio can be estimated as in Reali *et al.* (2017), from the sum of two contributions: Brownian motion and hydrodynamic diffusion of the individual grains due to their long-range interactions, which yields $\tau = \kappa_c/\kappa_T = k_B T_m/6\pi\mu r\kappa_T + (r/b)W_{st}$. The first term dominates for submicron particles, while the second term becomes important for larger sediment grains. Using the above estimates, the Rayleigh number Ra can be calculated to range from 7.2×10^{-11} to 3.7×10^{-3}.

3. Linear stability analysis

By decomposing the velocity, temperature and sediment-concentration fields into base states and perturbations, we can linearize (2.1)–(2.4) to obtain

$$u + \frac{\partial p}{\partial x} = 0, \quad w + \frac{\partial p}{\partial z} - Ra(T - C) = 0, \tag{3.1a,b}$$

$$\frac{\partial T}{\partial t} + \phi u + w - \nabla^2 T = 0, \tag{3.2}$$

https://doi.org/10.1017/jfm.2018.215 Published online by Cambridge University Press

$$\frac{\partial C}{\partial t} + \phi u + \frac{1}{R_\rho} w - W_{st}\frac{\partial C}{\partial z} - \tau \nabla^2 C = 0, \tag{3.3}$$

$$\frac{\partial u}{\partial x} + \frac{\partial w}{\partial z} = 0. \tag{3.4}$$

Elimination of the pressure by introducion of the vorticity variable yields

$$\Omega - Ra\frac{\partial}{\partial x}(T - C) = 0, \quad \Omega = \frac{\partial w}{\partial x} - \frac{\partial u}{\partial z}, \tag{3.5}$$

which demonstrates that the presence of vorticity is associated with horizontal temperature and sediment-concentration gradients.

The employment of normal modes $(u, w, T, C) \sim \mathrm{Re}[(\hat{u}, \hat{w}, \hat{T}, \hat{C})\exp(\lambda t + \mathrm{i}lx + \mathrm{i}kz)]$ allows us to rewrite (3.2)–(3.5) in terms of the eigenfunctions $(\hat{u}, \hat{w}, \hat{T}, \hat{C})$ and the vertical and horizontal real wavenumbers (k, l) to obtain a quadratic equation for the complex growth rate λ, where $K^2 = k^2 + l^2$,

$$\lambda^2 + a_1\lambda + a_2 = 0, \tag{3.6}$$

$$a_1 = K^2(1+\tau) + \frac{Ra\, l^2}{K^2}\left(1 - \frac{1}{R_\rho}\right) - \mathrm{i}kW_{st}, \tag{3.7}$$

$$a_2 = \tau K^4 + Ra\, l^2\left(\tau - \frac{1}{R_\rho}\right) + Ra\, l\phi k(1-\tau) - \mathrm{i}kW_{st}\left[\frac{Ra\, l}{K^2}(l - \phi k) + K^2\right]. \tag{3.8}$$

We can relate this result to the linear stability analyses of Rudraiah *et al.* (1982) and Alsinan *et al.* (2017). The former conducted an analysis of a two-component fluid in a saturated porous layer based on an extended version of Darcy's law that included inertial effects, while the latter considered the Navier–Stokes equations in stratified fluids. Both analyses yielded cubic polynomials for the growth rate, which reduce to quadratic forms if the inertial terms in the momentum equation are neglected, or in the limit of infinite Prandtl number. In addition, the current result reduces to that of Rudraiah *et al.* (1982) when $\phi = 0$ and $W_{st} = 0$. The above quadratic expression enables us to obtain exact forms of the neutral stability curves and to investigate limiting behaviours.

For the general case in which $W_{st} \neq 0$, an implicit relationship for the neutral stability curve can be obtained by setting the real part of the growth rate to zero, $\lambda_R = 0$. This criterion can be obtained by combining the roots of the quadratic equation (3.6) with an explicit representation of the square root of a complex number, i.e. by simplifying $\mathrm{Re}(\sqrt{\Delta}) = (1/\sqrt{2})[(\mathrm{Re}(\Delta)^2 + \mathrm{Im}(\Delta)^2)^{1/2} + \mathrm{Re}(\Delta)]^{1/2} = \mathrm{Re}(a_2)$, where $\Delta = a_1^2 - 4a_2$,

$$W_{st}^2 k^2\left[K^2(\tau - 1) + \frac{Ra\, l^2}{K^2}\left(2\frac{k}{l}\phi - 1 - \frac{1}{R_\rho}\right)\right]^2 = \left[K^2(1+\tau) + \frac{Ra\, l^2}{K^2}\left(1 - \frac{1}{R_\rho}\right)\right]^2$$
$$\times\left[4\tau K^4 + 4\, Ra\, l^2\left(\tau - \frac{1}{R_\rho}\right) + 4\, Ra\, l\phi k(1-\tau) + W_{st}^2 k^2\right]. \tag{3.9}$$

In the following, we use the above equations to investigate how the dimensionless governing parameters influence the onset of double-diffusive and settling-driven instabilities.

https://doi.org/10.1017/jfm.2018.215 Published online by Cambridge University Press

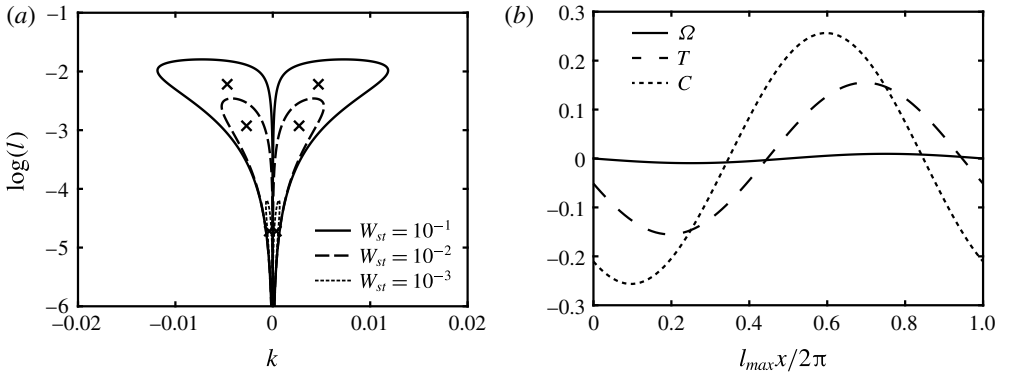


FIGURE 2. For $(Ra, \tau, R_\rho, \phi) = (10^{-3}, 1, 1.5, 0)$. (*a*) Neutral stability curve, $\lambda_R = 0$, as a function of the vertical and horizontal wavenumbers k and l, for different values of W_{st}. Pairs of wavenumbers $(\pm k, l)$ bounded by these contours have positive real parts of the growth rate, λ_R, and their corresponding maximum values are marked with an '×'. (*b*) Horizontal cross-sections, $z = 0$, of the normalized eigenfunctions, Ω, T and C for $W_{st} = 10^{-1}$. For visualization purposes, the amplitudes of the T and C eigenfunctions are multiplied by 10^{-4}. The settling velocity creates a phase shift between the temperature and sediment-concentration perturbations. This corresponds to a phase shift between stabilizing T and destabilizing C waves that drives unstable growth.

3.1. *Settling-driven instability*

We begin by considering the case $\tau = 1$, so that temperature and sediment diffuse at the same rate and double-diffusive instabilities are absent. In addition, we eliminate horizontal base state gradients by setting $\phi = 0$. In this configuration, the only potentially destabilizing mechanism is provided by the settling velocity. The corresponding Navier–Stokes situation was investigated by Alsinan *et al.* (2017), who found that the settling velocity creates a destabilizing phase shift between the T and C perturbations. We observe a similar behaviour in the current Darcy environment, which again triggers the growth of inclined waves.

Figure 2(*a*) shows the neutral stability curve, $\lambda_R = 0$, as a function of the vertical and horizontal wavenumbers k and l, for different values of the settling velocity W_{st} and $(Ra, \tau, R_\rho, \phi) = (10^{-3}, 1, 1.5, 0)$. Positive λ_R values are found inside these contours, and the fastest growing modes are marked by an '×'. Symmetry across the $k = 0$ line reflects the inclined nature of the settling-driven unstable waves. The phase shift between the T and C waves responsible for instability growth is shown in the horizontal cross-sections of the normalized eigenfunctions of Ω, T and C in figure 2(*b*).

The dependence of the growth rate and wavenumbers of the settling-driven instability on the density ratio is shown in figure 3. For constant W_{st}, $\lambda_{R,max}$ decreases with increasing R_ρ, since the overall density gradient becomes more stable. For large settling velocities, $\lambda_{R,max} \sim R_\rho^{-1}$, cf. figure 3(*a*), as λ_R approaches the limiting behaviour,

$$\lambda_R(W_{st} \to \infty) = \frac{Ra\, l}{K^2}\left(\frac{l}{R_\rho} - k\phi\right) - \tau K^2. \tag{3.10}$$

The imaginary part of the growth rate shown in figure 3(*b*) increases monotonically with the settling velocity, indicating a growing phase shift between T and C waves.

https://doi.org/10.1017/jfm.2018.215 Published online by Cambridge University Press

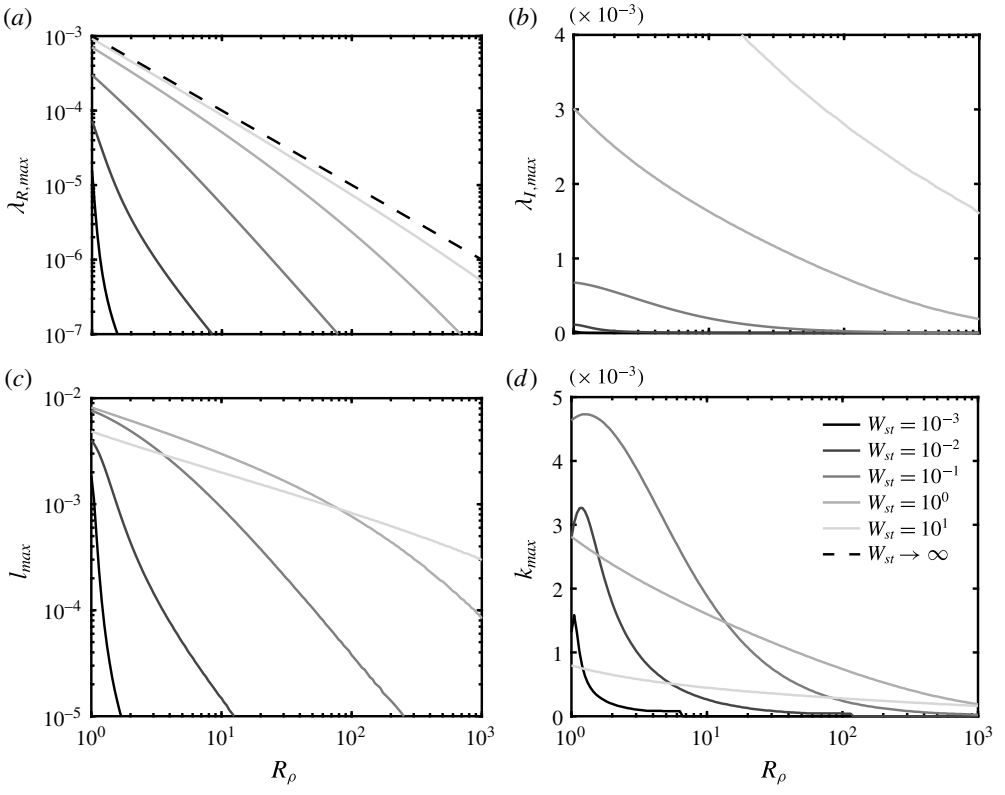


FIGURE 3. Properties of the fastest growing mode as a function of the density ratio R_ρ for a wide range of W_{st} and $(Ra, \tau, \phi) = (10^{-3}, 1, 0)$. Temperature and sediment diffuse at the same rate, so that the instability is purely settling-driven. (*a*) Real part of the maximum growth rate, $\lambda_{R,max}$, for different W_{st} values, for large settling velocities, $\lambda_{R,max} \sim R_\rho^{-1}$. (*b*) The imaginary part $\lambda_{I,max}$ of the fastest growing mode, indicative of the wave velocity, increases with W_{st}. (*c*) The horizontal wavenumber of the fastest growing mode decreases with R_ρ and increases with W_{st}, until it peaks near $W_{st} \approx 0.35$. (*d*) The dominant vertical wavenumber increases with W_{st} up to $W_{st} \approx 0.11$.

Figures 3(*c*) and 3(*d*), however, indicate that both the horizontal and the vertical wavenumbers reach maxima at moderate W_{st} values.

We proceed to the case of $\tau = 0.1$, for which the thermal diffusivity is larger than the sediment diffusivity. Now, both double-diffusive and settling-driven instabilities are present, so that we can investigate their interaction. Figure 4(*a*) shows the neutral stability curve as a function of the vertical and horizontal wavenumbers for increasing W_{st} values. Positive growth rates are found within the contours. For both $W_{st} = 0$ and $W_{st} = 0.05$, the maximum growth rate corresponds to the elevator mode $k = 0$, as indicated by two overlapping '×' symbols. For $W_{st} = 0.5$, the settling-driven instability mode dominates, giving rise to inclined waves.

Figure 4(*b*) shows the fastest growing vertical and horizontal wavenumbers as functions of W_{st}. Beyond a critical value of the settling velocity, $W_{st,crit} \approx 0.06$, the settling-driven instability mode dominates, marking the transition from elevator mode to inclined waves. Consequently, k_{max} increases beyond $W_{st,crit}$, peaks near $W_{st,peak} \approx 0.09$ and subsequently decreases, asymptotically approaching zero as

https://doi.org/10.1017/jfm.2018.215 Published online by Cambridge University Press

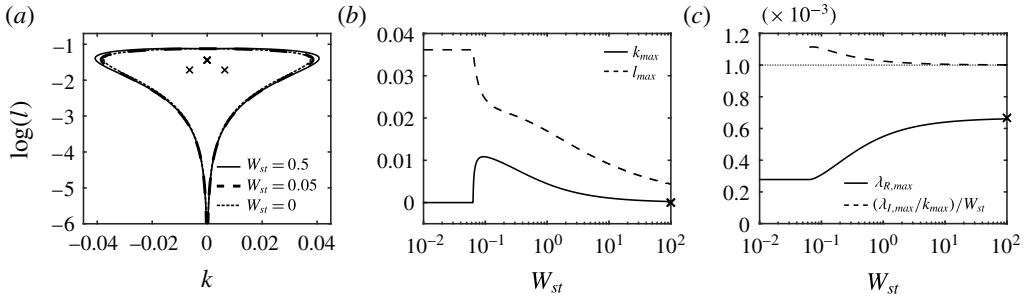


FIGURE 4. For $(Ra, \tau, R_\rho, \phi) = (10^{-3}, 0.1, 1.5, 0)$. (*a*) Neutral stability curve as function of k and l, for different W_{st} values. Positive growth rates exist within the contours. For both $W_{st} = 0$ and $W_{st} = 0.05$, only the double-diffusive instability is active, and the elevator mode $k = 0$ is most amplified. Beyond a critical W_{st} value, the settling-driven mode becomes dominant, so that the fastest growing waves are inclined. (*b*) Fastest growing vertical (k_{max}) and horizontal (l_{max}) wavenumbers as functions of W_{st}. Beyond a critical value of the particle settling velocity, $W_{st,crit} \approx 0.06$, the dominant instability mode changes from $k = 0$ to inclined waves. The symbols indicate limiting values as $W_{st} \to \infty$. (*c*) The most unstable growth rate and the normalized vertical phase velocity as functions of W_{st}. Here, $\lambda_{R,max}$ monotonically increases beyond $W_{st,crit}$ and asymptotically approaches $\lambda_R = (2/3) \times 10^{-3}$. The vertical phase velocity approaches the particle settling velocity for large W_{st} values. For visualization purposes, the values of $\lambda_{I,max}$ are multiplied by 10^{-3}.

$W_{st} \to \infty$, as indicated by the symbol '$\times$'. Beyond $W_{st,crit}$, l_{max} decreases monotonically, indicating a shift to longer waves as W_{st} increases. Figure 4(*c*) shows the maximum value of the real part of the growth rate, along with the normalized vertical phase velocity, as functions of W_{st}. Beyond $W_{st,crit}$, $\lambda_{R,max}$ increases monotonically, and it asymptotically approaches $\lambda_R = Ra(1/R_\rho - \phi) = (2/3) \times 10^{-3}$ for $W_{st} \to \infty$, $k_{max} \to 0$ and $l_{max} \to 0$. The vertical phase velocity asymptotically approaches the particle settling velocity for large W_{st}.

3.2. *Influence of lateral gradients*

In figure 5, we analyse how lateral base state gradients modify the case $(Ra, \tau, R_\rho, W_{st}) = (10^{-3}, 1, 1.5, 10^{-2})$, which we had investigated in figure 2(*a*). Figure 5(*a*) clearly demonstrates how the symmetry of the two lobes is broken for $\phi = 0.04$. A new intrusive instability mode is observed for small k values, similar to the situation in Navier–Stokes flows (Ruddick & Richards 2003; Medrano, Garaud & Stellmach 2014). This intrusive instability mode possesses smaller wavenumbers than the waves of the dominant settling-driven instability branch and triggers the growth of waves that are inclined opposite to them. For $\phi = 0.2$, figure 5(*b*), the intrusive lobe further increases in area and magnitude, while the settling-driven lobe with $k > 0$ shrinks. At $\phi = 0.7$, figure 5(*c*), only the intrusive lobe remains for $k > 0$.

We now proceed to analyse how the fastest growing mode changes with the strength of the double-diffusive instability, the lateral gradients and the settling velocity, and discuss stability criteria. Whenever instability growth happens, driven by double diffusion, settling or a combination of these effects, a neutral stability curve will exist in the form of a bounded region in the (l, k) space, with the fastest growing modes lying inside the closed neutral stability curve. An example is the instability purely driven by settling discussed in figure 2(*a*), where instability is found for

https://doi.org/10.1017/jfm.2018.215 Published online by Cambridge University Press

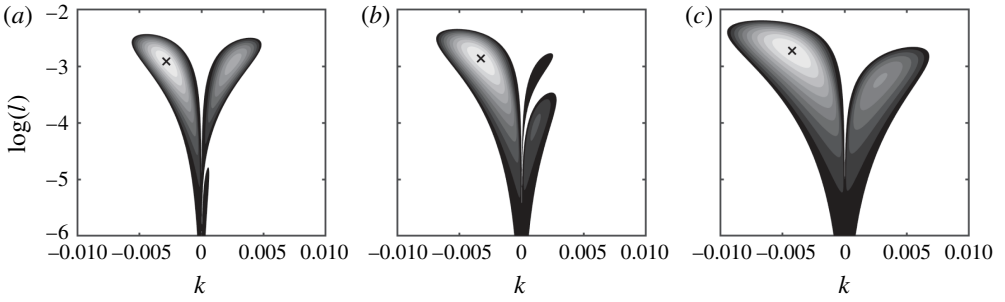


FIGURE 5. The positive real part of the growth rate as a function of the vertical, k, and horizontal, l, wavenumbers for $(Ra, \tau, R_\rho, W_{st}) = (10^{-3}, 1, 1.5, 10^{-2})$ and (a) $\phi = 0.04$, (b) $\phi = 0.2$, (c) $\phi = 0.7$. The most amplified mode is marked with an '$\times$'. Double-diffusive instabilities are absent and lateral base state gradients break the symmetry of the system, triggering a new intrusive instability mode.

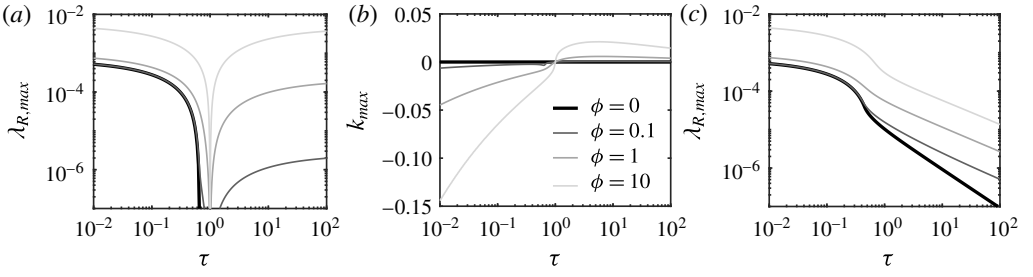


FIGURE 6. (a) The maximum real part of the growth rate, $\lambda_{R,max}$, and (b) the maximum vertical wavenumber, k_{max}, as functions of the diffusivity ratio τ for $W_{st} = 0$. (c) The maximum real part of the growth rate, $\lambda_{R,max}$, for $W_{st} = 10^{-2}$. The remaining parameters are $(Ra, R_\rho) = (10^{-3}, 1.5)$.

$W_{st} > 0$ and smaller positive W_{st} values reduce both the area of the neutral stability curve and the magnitude of the dominant modes. As a result, the existence of a neutral stability curve guarantees the existence of a dominant mode, and instability criteria for the dominant modes can be interpreted on the basis of the neutral stability relationships of (3.6).

For $W_{st} = 0$, figure 6(a) shows the maximum real part of the growth rate, $\lambda_{R,max}$, and figure 6(b) the maximum vertical wavenumber, k_{max}, as functions of the diffusivity ratio, τ, for different values of the lateral base state gradients. Figure 6(c) indicates the corresponding $\lambda_{R,max}$ for $W_{st} = 10^{-2}$. For $W_{st} = 0$, the growth rate is real and the neutral stability curve can be obtained by setting the coefficient $a_2 = 0$. This leads to

$$\tau K^4 = Ra\, l^2 \left(\frac{1}{R_\rho} - \tau \right) + Ra\, l\phi k(\tau - 1) > 0. \tag{3.11}$$

It should be noticed that if $\phi = 0$, the above equation is satisfied when $\tau < 1/R_\rho$. This instability criterion is consistent with previous experiments and linear stability results; cf. Cooper *et al.* (1997). In the presence of lateral gradients $\phi > 0$, and since the last term in (3.11) is always positive because k_{max} changes sign when τ crosses 1, instability can be seen whenever $\tau \neq 1$. This behaviour of k_{max} indicates that waves

https://doi.org/10.1017/jfm.2018.215 Published online by Cambridge University Press

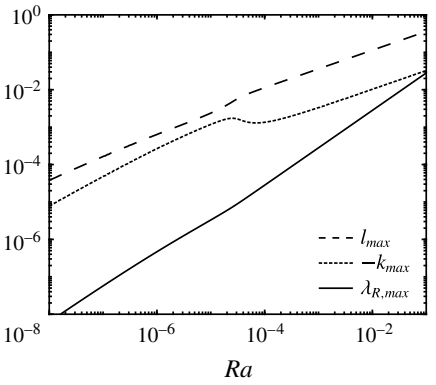


FIGURE 7. The maximum vertical, $-k_{max}$, and horizontal, l_{max}, wavenumbers and maximum real part of the growth rate, $\lambda_{R,max}$, for $(R_\rho, \tau, \phi, W_{st}) = (1.5, 0.1, 0.1, 10^{-2})$ as functions of the Rayleigh number. The maximum growth rate is approximately proportional to Ra.

are inclined in opposite directions if the thermal diffusivity is different from the sediment diffusivity. When $\tau = 1$, the above equation cannot be satisfied for $R_\rho \geqslant 1$, and the flow is stable regardless of the values of ϕ. This is expected since both double diffusion and settling velocity are absent. These results are consistent with the findings of Alsinan *et al.* (2017) for double-diffusive and settling-driven instabilities in Navier–Stokes environments.

The situation for $W_{st} = 1$ requires an analysis based on (3.9). Since many terms in this equation are squared, this equation can be satisfied whenever the last square bracket is non-negative, i.e.

$$4\tau K^4 + W_{st}^2 k^2 \geqslant 4\,Ra\,l^2\left(\frac{1}{R_\rho} - \tau\right) + 4\,Ra\,l\phi k(\tau - 1). \tag{3.12}$$

This equation does not impose any restriction on the parameters, and it is satisfied even when the right-hand side becomes negative. Consistent with this observation, instability is found for all values of τ and ϕ investigated; cf. figure 6(*c*).

Figure 7 shows how the maximum values of the real growth rate, along with the vertical and horizontal wavenumbers, change as a function of the Rayleigh number, Ra. The presence of positive lateral gradients renders the dominant vertical wavenumber negative. As suggested by (3.5), the maximum growth rate is approximately proportional to Ra. Larger wavenumbers grow faster as we increase vertical temperature gradients. This result is consistent with the stability criterion established by Nield (1968) for a fluid in an unbounded domain, where instability is expected for $Ra > 0$.

4. Conclusions

We have investigated the onset of instability in a stably stratified two-component fluid in a vertical Hele-Shaw cell, when the unstably stratified scalar has a settling velocity. Similarly to Navier–Stokes flows, this settling velocity triggers a new instability mode, which competes with the double-diffusive mode for unequal

https://doi.org/10.1017/jfm.2018.215 Published online by Cambridge University Press

diffusivities. Below a critical value of W_{st}, the double-diffusive elevator mode dominates, while, above this threshold, the inclined waves associated with the settling-driven instability exhibit faster growth. The analysis yields the neutral stability curves and allows for the discussion of various asymptotic limits. A natural extension of the current analysis will address the nonlinear evolution of these instabilities by means of direct numerical simulations.

Acknowledgement

The authors gratefully acknowledge financial support by NSF grant CBET-1438052.

References

ALSINAN, A., MEIBURG, E. & GARAUD, P. 2017 A settling-driven instability in two-component, stably stratified fluids. *J. Fluid Mech.* **816**, 243–267.

COOPER, C. A., GLASS, R. J. & TYLER, S. W. 1997 Experimental investigation of the stability boundary for double-diffusive finger convection in a Hele-Shaw cell. *Water Resour. Res.* **33** (4), 517–526.

COOPER, C. A., GLASS, R. J. & TYLER, S. W. 2001 Effect of buoyancy ratio on the development of double-diffusive finger convection in a Hele-Shaw cell. *Water Resour. Res.* **37** (9), 2323–2332.

DOBKINS, T. A. 1981 Improved methods to determine hydrodynamic fracture height. *J. Petrol. Tech.* **33** (04), 719–726.

GRIFFITHS, R. W. 1981 Layered double-diffusive convection in porous media. *J. Fluid Mech.* **102**, 221–248.

IMHOFF, P. T. & GREEN, T. 1988 Experimental investigation of double-diffusive groundwater fingers. *J. Fluid Mech.* **188**, 363–382.

KARIMI-FARD, M., CHARRIER-MOJTABI, M. C. & MOJTABI, A. 1999 Onset of stationary and oscillatory convection in a tilted porous cavity saturated with a binary fluid: linear stability analysis. *Phys. Fluids* **11** (1346), 1346–1358.

LIANG, F., SAYED, M., AL-MUNSTASHERI, G. A., CHANG, F. F. & LI, L. 2016 A comprehensive review on proppant technologies. *Petroleum* **2**, 26–39.

MEDRANO, M., GARAUD, P. & STELLMACH, S. 2014 Double-diffusive mixing in stellar interiors in the presence of horizontal gradients. *Astrophys. J. Lett.* **792** (L30), 1–5.

MURRAY, B. T. & CHEN, C. F. 1989 Double-diffusive convection in a porous medium. *J. Fluid Mech.* **201**, 147–166.

NIELD, D. A. 1968 Onset of thermohaline convection in a porous medium. *Water Resour. Res.* **4** (3), 553–560.

NIELD, D. A. & BEJAN, A. 2017 *Convection in Porous Media*. Springer.

PRINGLE, S. E. & GLASS, R. J. 2002 Double-diffusive finger convection: influence of concentration at fixed buoyancy ratio. *J. Fluid Mech.* **462**, 161–183.

PRINGLE, S. E., GLASS, R. J. & COOPER, C. A. 2002 Double-diffusive finger convection in a Hele-Shaw cell: an experiment exploring the evolution of concentration fields, length scales and mass transfer. *Trans. Porous Med.* **47**, 195–214.

RADKO, T. 2013 *Double-Diffusive Convection*. Cambridge University Press.

REALI, J. F., GARAUD, P., ALSINAN, A. & MEIBURG, E. 2017 Layer formation in sedimentary fingering convection. *J. Fluid Mech.* **816**, 268–305.

RUDDICK, B. & RICHARDS, K. 2003 Oceanic thermohaline intrusions: observations. *Prog. Oceanogr.* **56**, 499–527.

RUDRAIAH, N., SRIMANI, P. K. & FRIEDRICH, R. 1982 Finite amplitude convection in a two-component fluid saturated porous layer. *Intl J. Heat Mass Transfer* **25** (5), 715–722.

TAUNTON, J. W., LIGHTFOOT, E. N. & GREEN, T. 1972 Thermohaline instability and salt fingers in a porous medium. *Phys. Fluids* **15** (5), 748–753.

https://doi.org/10.1017/jfm.2018.215 Published online by Cambridge University Press

TRAXLER, A., GARAUD, P. & STELLMACH, S. 2011 Numerically determined transport laws for fingering ('thermohaline') convection in astrophysics. *Astrophys. J. Lett.* **728** (L29), 1–5.

TSAI, P. A., RIESING, K. & STONE, H. A. 2013 Density-driven convection enhanced by an inclined boundary: implications for geological CO_2 storage. *Phys. Rev.* E **87**, 011003(R).

TURNER, J. S. 1985 Multicomponent convection. *Annu. Rev. Fluid Mech.* **17**, 11–44.

VALKO, P. & ECONOMIDES, M. J. 1995 *Hydraulic Fracture Mechanics*. Wiley.

https://doi.org/10.1017/jfm.2018.215 Published online by Cambridge University Press